

# Band alignments and strain effects in PbTe/Pb<sub>1-x</sub>Sr<sub>x</sub>Te and PbSe/Pb<sub>1-x</sub>Sr<sub>x</sub>Se quantum-well heterostructures

M. Simma, G. Bauer, and G. Springholz\*

*Institut für Halbleiter und Festkörperphysik, Johannes Kepler Universität, A-4040 Linz, Austria*

(Received 8 September 2014; revised manuscript received 23 October 2014; published 18 November 2014)

The optical transitions and band alignments of PbTe/Pb<sub>1-x</sub>Sr<sub>x</sub>Te and PbSe/Pb<sub>1-x</sub>Sr<sub>x</sub>Se multi-quantum-well heterostructures were studied using temperature-modulated absorption spectroscopy and envelope function calculations. By taking advantage of the strain-induced splitting of conduction- and valence-band states at the different  $L$  points of the Brillouin zone, a reliable determination of the band offsets is obtained, taking into account the biaxial strain of the quantum wells derived by x-ray diffraction. Through this analysis, the normalized conduction-band offsets are determined as  $\Delta E_c/\Delta E_g = 0.45 \pm 0.05$  for the PbTe/Pb<sub>1-x</sub>Sr<sub>x</sub>Te system and  $0.6 \pm 0.1$  for the PbSe/Pb<sub>1-x</sub>Sr<sub>x</sub>Se system for Sr contents up to 13%. Within the experimental precision, the band offsets are independent of temperatures from 20–300 K. With these parameters, precise modeling of the energy levels and optical transitions is achieved as required for optoelectronic device applications.

DOI: [10.1103/PhysRevB.90.195310](https://doi.org/10.1103/PhysRevB.90.195310)

PACS number(s): 73.21.Fg, 73.61.Le, 78.67.De, 81.07.Vb

## I. INTRODUCTION

Lead salt heterostructures using Sr- or Eu-based ternary alloys have been widely employed for mid-infrared optoelectronic devices [1–14]. This is due to the large tunability of the ternary band gaps [14–18] arising from the very large band-gap difference between the narrow gap lead salt compounds and the wide gap Sr or Eu monochalcogenides [14]. As a result, for quantum well heterostructures, only moderate Sr or Eu concentrations are required to observe pronounced quantum confinement effects [14,19–25], and a wide range of devices such as vertical cavity surface emitting lasers [4–7], microdisk [8] and photonic crystal lasers [11], wavelength tunable external vertical cavity lasers [9,10], as well as resonant cavity detectors [12,13] has been demonstrated. In fact, PbSe/PbSrSe lasers have achieved the highest continuous-wave operation temperature of all type-I band-gap lasers in the mid-infrared region [8]. Recent work has also revealed a high potential of lead strontium telluride for thermoelectric devices [26–28], and lead tin chalcogenides were recently demonstrated as a new class of topological crystalline insulators, exhibiting topologically protected two-dimensional (2D) surface states with dispersion of a Dirac cone [29–32]. In addition, novel topological phases have been predicted in lead salt quantum-well and superlattice structures [33,34].

For band-gap engineering of quantum confined structures, the band alignment between quantum well and barrier materials is of fundamental importance as it determines the energy levels as well as optical matrix elements due to the wave-function overlap between the electrons and holes. While for Eu-based lead salt structures the band alignments have been studied in great detail [20–22], a great ambiguity exists for the Sr-based systems for which only qualitative results have been reported. For example, for the PbSe/PbSrSe system, a conduction-band offset of  $\Delta E_c/\Delta E_g = 0.82$  was suggested from photoluminescence evaluated by a simple Kronig-Penney model [24,25], whereas interband absorption measurements were modeled assuming a symmetric band alignment [23,35].

For PbTe/PbSrTe quantum wells, a type-I band alignment was concluded from laser data [17], but no information on the exact band offset value was obtained. As previously shown [20–22,36], for band offset determination from interband optical transitions, the analysis of transitions close to the barrier band gap is essential because the ground-state transitions are insensitive to the band alignments. In the narrow gap lead salt compounds, however, these higher-energy transitions are strongly affected by the nonparabolicity of the electronic band structure, which therefore needs to be taken into account.

In the present work, we employ an envelope function model with energy-dependent effective masses derived from six-band  $\mathbf{k} \cdot \mathbf{p}$  calculations to analyze the full spectrum of optical transitions in multi-quantum-well structures to quantitatively derive the band alignments of the two technologically important PbTe/Pb<sub>1-x</sub>Sr<sub>x</sub>Te and PbSe/Pb<sub>1-x</sub>Sr<sub>x</sub>Se heterostructure systems. A whole series of samples was studied for both systems and the influence of strain was taken into account by the deformation potentials. With the input of precise structural data from x-ray diffraction and of band parameters derived from magneto-optical experiments [37–39], we determine the normalized conduction-band offset as  $\Delta E_c/\Delta E_g = 0.45 \pm 0.05$  for the PbTe/PbSrTe system and  $0.6 \pm 0.1$  for the PbSe/PbSrSe system for the whole temperature range from 20 to 300 K and Sr contents  $x_{\text{Sr}}$  up to 13%. Strain effects are demonstrated to be significant in the PbTe system, leading to significant shifts of the energy levels and modifications of the valley splitting. This strain sensitivity yields a higher precision for the band alignments because two sets of optical transitions must be fitted simultaneously. For the PbSe system, strain effects are found to be less important due to the smaller deformation potentials as well as the lower strain values. With the band parameters derived here and our previous results obtained for the Eu-based systems [20–22], we establish a complete parameter set for realistic modeling of IV-VI heterostructures for optoelectronic device applications.

## II. GROWTH AND STRUCTURAL CHARACTERIZATION

The multi-quantum-well (MQW) samples were fabricated by molecular-beam epitaxy on (111) BaF<sub>2</sub> substrates

\*Corresponding author: [gunther.springholz@jku.at](mailto:gunther.springholz@jku.at)

using PbTe, PbSe, Sr, Se, and Te effusion cells [40]. The structures consist of 18–50 periods of PbTe/Pb<sub>1-x</sub>Sr<sub>x</sub>Te or PbSe/Pb<sub>1-x</sub>Sr<sub>x</sub>Te quantum wells grown onto 2–4  $\mu\text{m}$  fully relaxed Pb<sub>1-x</sub>Sr<sub>x</sub>Te or Pb<sub>1-x</sub>Sr<sub>x</sub>Se buffer layers having the same composition as the barrier layers. The quantum-well thickness was varied over a wide range from  $d_{\text{QW}} = 72\text{--}223$   $\text{\AA}$ , while the barrier thickness was kept constant at around 300  $\text{\AA}$  and the Sr content  $x_{\text{Sr}}$  was in the range of 11 to 14%. This yields relatively high barriers for the quantum wells, which significantly enhances the sensitivity for the band alignments because more energy levels are available for comparison between experiments and theoretical calculations and because the transitions close to the barriers depend more strongly on the band offsets compared to structures with lower Sr content. For  $x_{\text{Sr}} = 13\%$ , the Pb<sub>1-x</sub>Sr<sub>x</sub>Te band gap is as large as 523 meV compared to 225 meV for PbTe, and it is 458 meV for Pb<sub>1-x</sub>Sr<sub>x</sub>Se compared to 167 meV for PbSe at 77 K. All sample parameters are listed in Table I.

The thicknesses, strains, and compositions of the layers were precisely determined by high-resolution x-ray diffraction. This is essential for exact theoretical modeling of the electronic transitions as required for band offset determination. Representative (222) x-ray diffraction spectra are presented in Figs. 1(a) and 1(b) for PbTe/PbSrTe and PbSe/PbSrSe multi-quantum wells with  $d_{\text{QW}} = 72$   $\text{\AA}$  and 84  $\text{\AA}$ , respectively. In both cases, pronounced superlattice satellite peaks centered around the zero-order *SL0* reflection are observed, to the left of which the Bragg reflection of the buffer layer *B* appears. The Sr content was derived from the lattice constant of the relaxed buffer layer using Vegards law, interpolating linearly between the lattice constants of the binaries given by  $a_{\text{PbTe}} = 6.462$   $\text{\AA}$ ,  $a_{\text{PbSe}} = 6.126$   $\text{\AA}$ ,  $a_{\text{SrTe}} = 6.660$   $\text{\AA}$  [41], and  $a_{\text{SrSe}} = 6.236$   $\text{\AA}$  [42], respectively. From the satellite peak spacing and the Sr concentration, the exact QW and barrier thicknesses were obtained as listed in Table I.

Due to the increase of the lattice constant with increasing Sr content, a lattice mismatch exists between the binary quantum wells and the ternary barriers that for PbTe/PbSrTe amounts to  $\Delta a/a = 0.4\%$  for  $x_{\text{Sr}} = 14\%$ . As a result, a significant tensile strain is imposed on the QW layers. This strain was determined using high resolution x-ray reciprocal space mapping around the asymmetric (15 $\bar{3}$ ) Bragg reflection, as illustrated in Figs. 1(c) and 1(d) for two representative samples,

TABLE I. Structural parameters of the investigated PbTe/Pb<sub>1-x</sub>Sr<sub>x</sub>Te and PbSe/Pb<sub>1-x</sub>Sr<sub>x</sub>Se MQW samples derived from x-ray diffraction and FTIR measurements.  $d_{\text{QW}}$  and  $d_{\text{barr}}$  represent the QW and barrier thicknesses,  $x_{\text{Sr}}$  represents the Sr content in the barriers,  $\varepsilon_{\parallel, \text{QW}}$  is the in-plane QW strain, and  $N_{\text{SL}}$  is the number of MQW periods.

Sample	VA745	VA782	VA800	VA807	VA948	VA949
Material	PbTe/PbSrTe				PbSe/PbSrSe	
$d_{\text{QW}}$ ( $\text{\AA}$ )	72	147	190	223	84	138
$d_{\text{barr}}$ ( $\text{\AA}$ )	270	293	300	267	286	292
$x_{\text{Sr}}$ (%)	11.6	14.1	12.1	12.2	13.0	12.6
$\varepsilon_{\parallel, \text{QW}}$ (%)	0.31	0.43	0.29	0.25	0.11	0.10
$N_{\text{SL}}$ periods	50	24	18	16	40	23

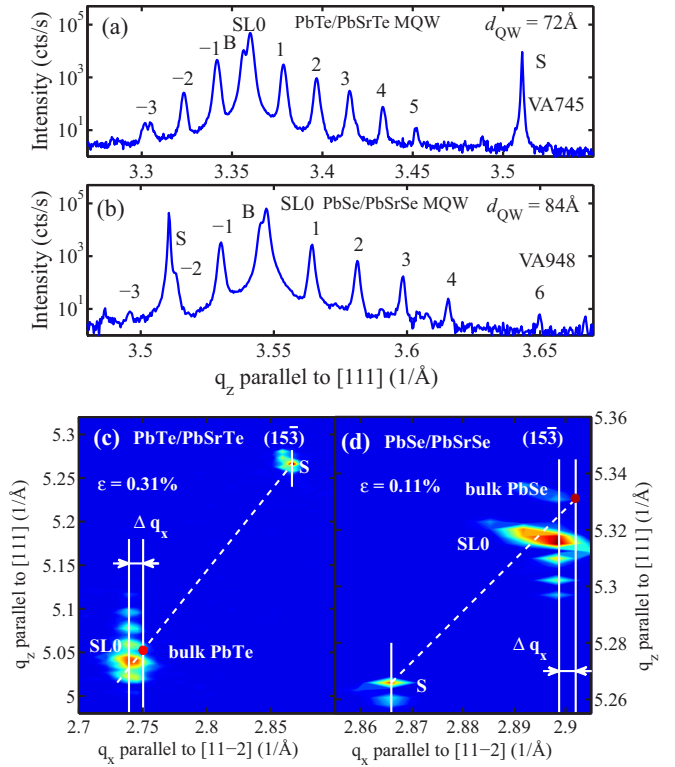


FIG. 1. (Color online) High-resolution (222) x-ray diffraction spectra of a (a) PbTe/PbSrTe and (b) PbSe/PbSrSe MQW with QW thicknesses of  $d_{\text{QW}} = 72$  and 84  $\text{\AA}$ , respectively. The peaks from the buffer layer, substrate, and the MQW stack are labeled by *B*, *S*, *SL0*, and  $\pm i$ . (c), (d) Reciprocal space maps of the samples around the asymmetric (15 $\bar{3}$ ) Bragg reflection, with the reciprocal space coordinates  $q_x$  and  $q_z$  parallel and perpendicular to the surface. The nominal position of bulk (15 $\bar{3}$ ) PbTe and PbSe reciprocal lattice points is indicated by (•). The structural parameters derived from these measurements are listed in Table I.

where the BaF<sub>2</sub> substrate peak “S” was used as reference for the reciprocal space coordinates ( $a_{\text{BaF}_2} = 6.200$   $\text{\AA}$ ). As indicated by the vertical lines, the MQW satellite peaks are laterally shifted by  $\Delta q_x$  with respect to the nominal bulk PbTe and PbSe peak positions marked by red dots (•) in Figs. 1(c) and 1(d). From this shift, the in-plane lattice constant of the MQW stack and, thus, the in-plane strain of the QWs was derived using  $\varepsilon_{\parallel, \text{QW}} = \Delta q_x / q_{x, \text{SL}}$ . The results are listed in Table I. For the PbTe QWs, the measured strain values are around 0.3%, whereas it is only around 0.1% for the PbSe wells. This is because the lattice constant difference between PbTe and SrTe ( $\Delta a/a = 3.06\%$ ) is about a factor-of-two larger compared to that between PbSe and SrSe (1.8%).

### III. MEASUREMENT OF INTERBAND TRANSITIONS

The interband transitions within the MQWs were derived by temperature-modulated differential transmission spectroscopy (DTS) [21,23]. In this technique, the infrared transmission  $\mathcal{T}(\omega)$  measured at two slightly different temperatures is subtracted from each other to obtain the differential transmission  $\Delta \mathcal{T}/\mathcal{T}$  at a given  $T$ . For our measurements, the temperature difference was chosen as  $\Delta T = 3$  K such that

the band gaps are modulated by  $\sim 1$  meV due to the temperature dependence of  $dE_g/dT \sim 0.4$  meV/K [see Eqs. (1) and (2) below]. As a result, sharp and distinct peaks appear at the onset of the quantum-well transitions in the DTS spectra [21]. Prior to these measurements, an impedance-matching NiCr antireflection layer was deposited on top of the samples, having a thickness of 470 and 550 Å for the PbTe/PbSrTe and PbSe/PbSrSe MQWs, respectively. As shown in detail in Refs. [21,43], in this way the pronounced multiple-reflection Fabry-Perot interference fringes resulting from the very large refractive index contrast between the lead salt epilayers and the BaF<sub>2</sub> substrate [20] can be suppressed. For all samples, differential transmission spectra were measured as a function of temperature between 20 and 300 K using Fourier-transformed infrared (FTIR) spectroscopy. From the absorption edge of the barriers determined by fitting the transmission spectra with the transfer matrix method [20,21], the temperature and  $x_{\text{Sr}}$  dependence of the band gaps  $E_g(x, T)$  were deduced. This yields the following expression for Pb<sub>1-x</sub>Sr<sub>x</sub>Te

$$E_g(x, T) = 196 + 0.440T^2 \frac{(1 - 3.63x)}{(T + 15.2)} + 2420x, \quad (1)$$

and for Pb<sub>1-x</sub>Sr<sub>x</sub>Se,

$$E_g(x, T) = 146 + 0.524T^2 \frac{(1 - 2.7x)}{(T + 68.8)} + 2300x, \quad (2)$$

for  $x_{\text{Sr}} \leq 15\%$ . In these expressions, the band gaps  $E_g$  are given in meV and  $x$  is the Sr concentration derived from the Vegards law. At room temperature, the bands gaps vary as  $dE_g/dx = 1.96$  for PbSrTe and 1.95 eV for PbSrSe. At 4 K, the corresponding values are  $dE_g/dx = 2.42$  and 2.3 eV, respectively. The strong increase of  $E_g$  with  $x$  is due to the large band gaps of SrTe and SrSe of 3 and 3.8 eV, respectively [44,45], which, however, are indirect at  $\Gamma$ -X of the Brillouin zone.

For the PbTe/PbSrTe MQWs, the differential transmission spectra at 80 K are shown in Figs. 2(a)–2(c) for  $d_{\text{QW}} = 72$ , 147, and 190 Å, respectively. Corresponding results for the PbSe/PbSrSe MQWs are shown in Fig. 3. In the DTS spectra, the peaks at the onset of the QW transitions are indicated by arrows and labeled by  $E_{ii}^{l,o}$ , where  $i$  refers to the quantum number of the initial and final state of the optical transition and the superscript to the pertaining valley of the band structure. Due to the many-valley band structure of PbTe and PbSe with the extrema at the  $L$  points of the Brillouin zone [46], the energy levels in (111)-oriented QWs split up into two independent sublevel systems—one for the longitudinal valley ( $l$ ) with the long axis of the effective mass ellipsoid perpendicular to the surface, and one for the three oblique  $L$  valleys ( $o$ ) with the valley axes inclined by  $70.5^\circ$  to the growth direction [see inset in Fig. 2(a)]. In Figs. 2 and 3, the corresponding longitudinal and oblique interband transitions are indicated by blue and red colors, respectively.

For the PbTe MQW with the thinnest quantum wells [ $d_{\text{QW}} = 72$  Å; Fig. 2(a)], only the ground-state  $E_{11}$  transition is observed for both valleys, whereas for the longitudinal valley also two excited-state transitions up to  $E_{33}^l$  appear. This difference is due to the very large effective mass anisotropy in PbTe with  $m_{\parallel}/m_{\perp} = 9.15$  for electrons and 9.74 for holes in the direction parallel and perpendicular to the  $\langle 111 \rangle$  valley axes

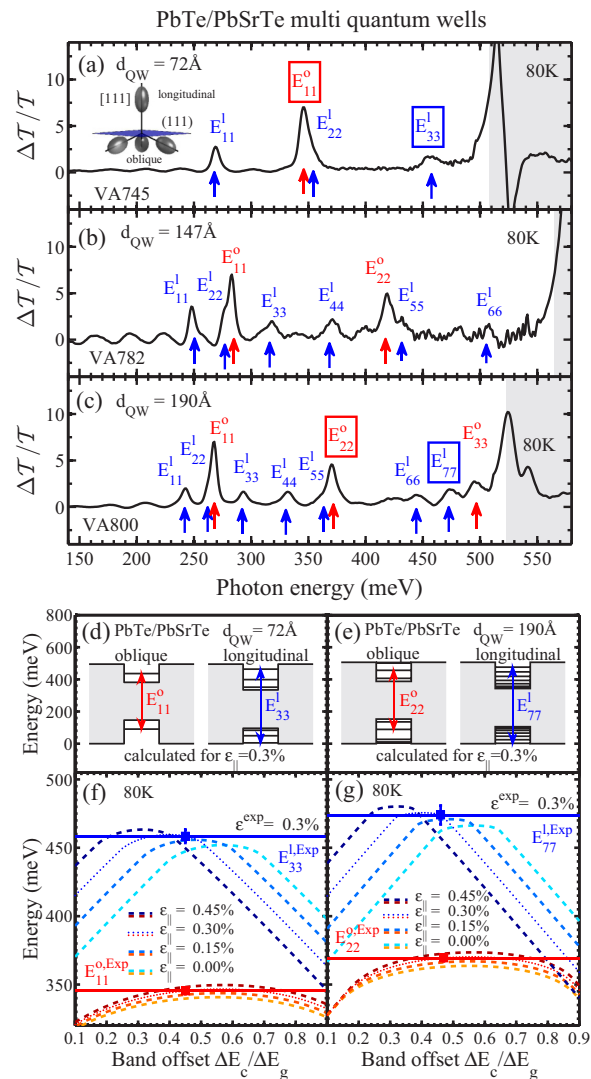


FIG. 2. (Color online) Differential transmission spectra  $\Delta T/T$  of three PbTe/PbSrTe MQWs with  $d_{\text{QW}} =$  (a) 72 Å, (b) 147 Å, and (c) 190 Å measured at  $T = 80$  K. The peaks arising from the  $i$ - $i$  QW transitions in the longitudinal ( $l$ ) and oblique ( $o$ ) valleys are indicated by the blue and red arrows, respectively, and the shaded regions mark the energy range above the barrier band gap. (a) Inset: Orientation of the effective mass ellipsoids of the longitudinal and three oblique  $L$  valleys with respect to the  $\langle 111 \rangle$  QW plane. (f),(g) Calculated transition energies (dashed lines) in dependence of the normalized unstrained conduction-band offset  $\Delta E_c/\Delta E_g$  for  $d_{\text{QW}} = 72$  and 190 Å, respectively. The corresponding transitions are indicated by the boxes in (a) and (b). The transition energies were calculated for four different QW strain values  $\epsilon_{\parallel, \text{QW}} = 0, 0.15, 0.3$ , and 0.45%, where  $\epsilon^{\text{exp}} = 0.3\%$  (dotted line) is the experimental value. The measured transition energies  $E_{ii}^{(\text{exp})}$  are represented by the horizontal lines and the squares (■) mark the intersection with the theoretical curves. This yields the unstrained band alignment as  $\Delta E_c/\Delta E_g = 0.45 \pm 0.05$ . (d), (e) Derived strained band profiles for each valley type.

at 80 K. As a result, the effective mass  $m_z$  in the quantization direction is about three times larger for the longitudinal valley, i.e., the transitions are redshifted with respect to those of the oblique valleys. As shown by Figs. 2(b) and 2(c), for thicker

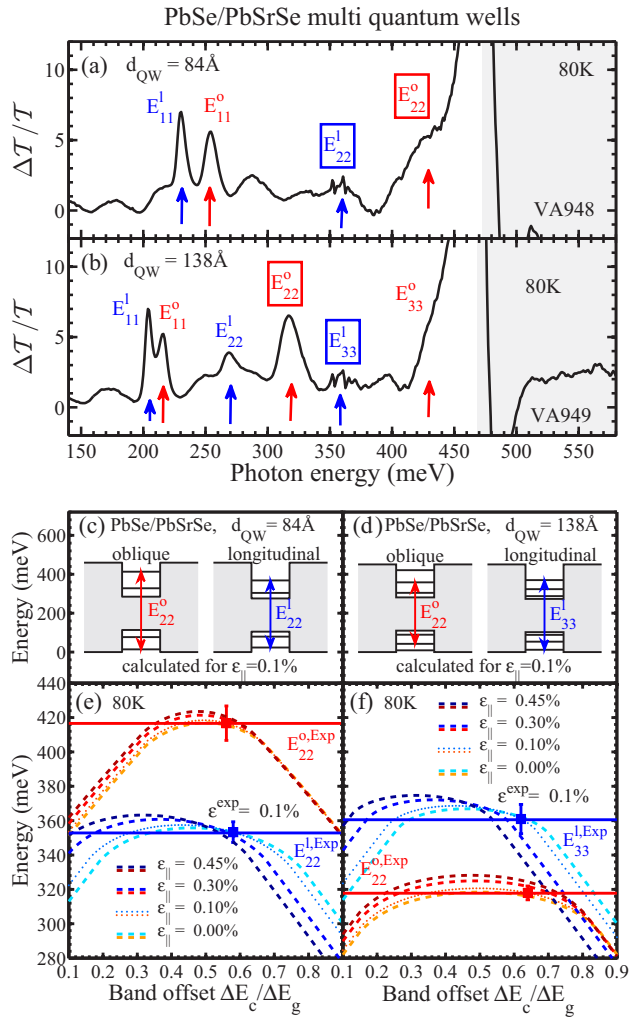


FIG. 3. (Color online) Differential transmission spectra  $\Delta T/T$  of two PbSe/PbSrSe MQW samples with  $d_{\text{QW}} =$  (a) 84 Å and (b) 138 Å measured at  $T = 80$  K. The peaks arising from the  $E_{ii}^{(l,o)}$  quantum-well transitions in the longitudinal ( $l$ ) and oblique ( $o$ ) valleys are indicated by the blue and red arrows, respectively, and the shaded regions mark the energy range above the barrier band gap. (e), (f) Calculated transition energies plotted in dependence of the normalized unstrained conduction band offset  $\Delta E_c/\Delta E_g$  (dashed/dotted lines) for the highest QW transitions  $E_{ii}^{(l,o)}$  in both samples. The lines were calculated for four different tensile QW strain values  $\epsilon_{\parallel, \text{QW}} = 0, 0.15, 0.3$ , and  $0.45\%$ , where  $\epsilon^{\text{exp}} = 0.1\%$  (dotted line) is the value determined by x-ray diffraction. The measured transition energies  $E_{ii}^{(\text{exp})}$  are represented by the horizontal solid lines and the squares (■) mark the intersection with the calculated values curves. This yields  $\Delta E_c/\Delta E_g = 0.6 \pm 0.1$  for this system. (c), (d) Derived strained band profiles for each valley type.

QWs, the transitions shift to lower energies and more and more energy levels become confined. Thus, for the  $d_{\text{QW}} = 190$  Å sample, transitions up to  $E_{33}^o$  and  $E_{77}^l$  appear.

Similar features are seen for the PbSe/PbSrSe MQWs [cf. Figs. 3(a) and 3(b)] where for the thinner QWs, only transitions between the ground and first excited state occur, whereas for the thicker QWs, transitions up to  $E_{33}^o$  appear. It is noted that the valley splitting ( $E_{ii}^l - E_{ii}^o$ ) in the PbSe QWs is clearly much

smaller than for the PbTe wells. This is due to the five-times-lower effective mass anisotropy of PbSe of  $m_{\parallel}/m_{\perp} = 1.85$  (electrons) and 1.64 (holes) at 80 K. In both systems, the valley splitting decreases with increasing QW thickness. For the ground state transition, the splitting decreases from 80 meV at  $d_{\text{QW}} = 72$  Å to 25 meV at  $d_{\text{QW}} = 190$  Å for PbTe, and from 25 to 10 meV for PbSe when  $d_{\text{QW}}$  increases from 84 to 138 Å. It is also noted that due to the threefold valley degeneracy, the DTS peaks of the oblique valley transitions are significantly higher than those for the longitudinal valleys.

#### IV. THEORETICAL MODELING

An envelope function approach [2,14,19] is employed to calculate the energy levels in the quantum wells in dependence of well thicknesses, strain, Sr content, and temperature, while varying the band offset between the QW and barrier materials. The confining potentials  $V(z)$  for the electrons and holes are set by the conduction- and valence-band offsets, where  $V(z)$  is set to zero within the QWs and to  $\Delta E_c = \xi \Delta E_g$  and  $\Delta E_v = (1 - \xi) \Delta E_g$  in the barriers.  $\xi = \Delta E_c/\Delta E_g$  represents the normalized unstrained ( $\epsilon_{\parallel} = 0$ ) conduction-band offset that is used as the variable parameter in our calculations. The temperature and  $x_{\text{Sr}}$  dependence of the QW and barrier band gaps are incorporated using Eqs. (1) and (2), and the effect of strain is taken into account through the deformation potentials, as described below. For the resulting confining potentials, the QW energy levels are calculated by solving the Schrödinger equation with the Hamilton operator as given in Refs. [19,22].

To account for the strong band nonparabolicity of the lead salt compounds, energy-dependent effective masses derived from magneto-optical experiments and six-band  $\mathbf{k} \cdot \mathbf{p}$  envelope function approximation calculations are used [2,14,37,38]. In this approach, the longitudinal ( $\parallel$ ) and transversal ( $\perp$ ) effective masses parallel and perpendicular, respectively, to the  $\langle 111 \rangle$  valley axes are represented by

$$\frac{1}{m_{\parallel, \perp}^{c,v}(|E_n|)} = \frac{2}{m_0^2} \frac{P_{\parallel, \perp}^2}{(|E_n| \pm E_g^*)} + \frac{1}{m_{\perp, \parallel}^{\pm}}, \quad (3)$$

where  $P_{\parallel, \perp}$  denotes the momentum matrix elements parallel and perpendicular to the  $\langle 111 \rangle$  directions,  $E_n$  denotes the eigenenergies of the quantum-well states with respect to the QW band edges, and  $m_{\perp, \parallel}^{\pm}$  denotes the far band contributions in the conduction ( $-$ ) and valence ( $+$ ) bands as listed in Table II. Thus, the Schrödinger equation has to be solved self-consistently. In the above equation,  $E_g^*$  represents a renormalized band gap and is given by  $E_g^* = E_{g, \text{QW}}$  within the QWs and by  $E_g^* = \frac{1}{2}[E_{g, \text{QW}} + E_{g, \text{barr}} \mp (\Delta E_c - \Delta E_v)]$  in the barriers [19], where the term  $(\Delta E_c - \Delta E_v)$  represents the shift of the midgap position in the barriers with respect to that in the QWs. It is noted that the temperature dependence of the effective masses is encoded in the temperature dependence of the band gaps  $E_g(x, T)$ , as given by Eqs. (1) and (2). For the longitudinal valley, the confinement mass  $m_z$  in the growth direction is simply equal to  $m_{z,l}^{c,v} = m_{\parallel}^{c,v}$ , whereas for the oblique valleys,  $m_{z,o}^{c,v} = 9m_{\perp}^{c,v}m_{\parallel}^{c,v}/(m_{\perp}^{c,v} + 8m_{\parallel}^{c,v})$ .

In the biaxially strained  $\langle 111 \rangle$  QWs, the effect of strain on the position of the QW band edges with respect to those of the

TABLE II. Band parameters [20,37] and deformation potentials of PbTe and PbSe at 4 K used for the envelope function calculations. Also listed are the unstrained band offsets  $\Delta E_c/\Delta E_g$  of the PbTe/PbSrTe and PbSe/PbSrSe system obtained in this work.

Material	$E_g$	$\frac{2P_{\perp}^2}{m_0}$	$\frac{P_{\perp}}{P_{\parallel}}$	$\frac{m_{\perp}^-}{m_0}$	$\frac{m_{\parallel}^-}{m_0}$	$\frac{m_{\perp}^+}{m_0}$	$\frac{m_{\parallel}^+}{m_0}$	Refs.	$D_d^c$	$D_u^c$	$D_d^v$	$D_u^v$	$\Delta E_c/\Delta E_g$
PbTe	189.7	6.02	3.42	0.060	0.505	0.102	0.920	[20]	-4.4	8.3	-7.6	8.9	$0.45 \pm 0.05$
PbSe	146.3	3.6	1.96	0.27	0.95	-0.29	-0.37	[37]	-4.2	4.2	-7.4	3.9	$0.6 \pm 0.1$

unstrained barriers is accounted for by the relations [47]

$$\delta E_l^{c,v} = D_d^{c,v}(2\varepsilon_{\parallel} + \varepsilon_{\perp}) + D_u^{c,v}\varepsilon_{\perp}, \quad (4)$$

$$\delta E_o^{c,v} = D_d^{c,v}(2\varepsilon_{\parallel} + \varepsilon_{\perp}) + D_u^{c,v}(8\varepsilon_{\parallel} + \varepsilon_{\perp})/9, \quad (5)$$

where  $\delta E_{o,l}^{c,v}$  are the energy shifts of the band edges induced by strain,  $D_{d,u}^{c,v}$  are the deformation potentials listed in Table II, and  $\varepsilon_{\parallel}$  and  $\varepsilon_{\perp}$  are the in-plane and out-of-plane strain tensor components, respectively. For (111)-oriented epilayers, these are related through the elastic constants  $C_{ij}$  as

$$\varepsilon_{\perp} = -2(C_{11} + 2C_{12} - 2C_{44})/(C_{11} + 2C_{12} + 4C_{44})\varepsilon_{\parallel}. \quad (6)$$

In our structures, strain is exclusively imposed on the QWs due to their pseudomorphic growth on fully relaxed buffer layers having the same ternary composition as the barrier layers. Thus, the resulting tensile QW strain is of the order of 0.3% and 0.1% for the PbTe/PbSrTe and PbSe/PbSrSe structures, respectively, with the actually measured values listed in Table I.

Using the above relations, one finds that strain strongly affects the band-edge positions for the longitudinal valley [Eq. (4)], but only weakly those of the oblique valleys [Eq. (5)]. For the PbTe QWs, the  $\varepsilon_{\parallel} = +0.3\%$  tensile strain leads to a downward shift of the longitudinal band edges by  $\delta E_l^c = -39$  eV, whereas for the oblique valleys, there is only a small upward shift of  $\delta E_o^c = +7$  meV. For the PbSe QWs, the shifts are significantly smaller due to the two times smaller strain values and smaller deformation potentials (see Table II). Thus, the downward shift for the longitudinal valley is only  $-8$  meV and the shift of the oblique valleys only  $-0.3$  meV. The tensile strain also increases the QW band gaps by  $\delta E_g^l = \delta E_l^c - \delta E_l^v = +11$  meV and  $\delta E_g^o = +8$  meV for PbTe, whereas for PbSe, the gap increases only by about  $+2$  meV for both valleys.

Upon cooling to cryogenic temperatures, an additional small tensile *thermal* strain is induced in the whole MQW stack due to the small, but not completely negligible, difference in the thermal-expansion coefficient between the BaF<sub>2</sub> substrate and the lead salt epilayers. However, even at low temperatures, this thermal strain is less than 0.1% and, thus, its influence on the band gaps is rather small (below 2 meV). In fact, this has already been taken into account in the band-gap relations  $E(x, T)$  of Eqs. (1) and (2), which were determined from reference layers on BaF<sub>2</sub> (111) substrates, where the same thermal strain is induced. It is noted, however, that the thermal strain is imposed equally on the QWs and barrier materials. As a result, the thermal strain does not influence the relative band alignments in the MQW structures—contrary to the lattice-mismatch strain, which is present only in the QWs but not in the barriers. Thus, the thermal strain does not need

to be taken into account in Eqs. (4) and (5), contrary to the assumptions put forward, e.g., in Ref. [47].

## V. DETERMINATION OF THE BAND OFFSETS

To derive the band offsets in our heterostructures, all transition energies between the confined quantum-well states were calculated as a function of the unstrained conduction-band offset between the well and barrier materials. For the PbTe/PbSrTe MQWs with  $d_{\text{QW}} = 72$  Å and 138 Å, the transition energies of the two highest optical transitions are plotted in Figs. 2(f) and 2(g) as dashed/dotted lines versus  $\Delta E_c/\Delta E_g$ , where the different lines are calculated for different QW strains  $\varepsilon_{\parallel, \text{QW}}$  varied between 0 and 0.45% as indicated. Again, the transition energies for the oblique and longitudinal valleys are represented by the red and blue lines, respectively. Evidently, the transition energies exhibit a maximum for a nearly symmetric band alignment  $\Delta E_c/\Delta E_g \approx 0.5$ . This is due to the nearly equal electron and hole masses of the lead salt compounds. With increasing band offset asymmetry the transition energies decrease in both directions because the reduction of the quantization energy due to the decrease in the barrier height in either the valence or conduction band is not fully compensated by a comparable increase in the opposite band.

The influence of strain is demonstrated by the curves derived for different strain values. One can see that with increasing tensile strain, the maxima of the curves for the longitudinal transitions (blue curves) shift to the left to smaller  $\Delta E_c/\Delta E_g$  values, whereas the curves for the oblique valleys mainly shift in the upward direction. This different behavior for the two types of valleys comes from the fact that for the longitudinal valley, strain mostly leads to a downward shift of the QW band edges relative to the unstrained barriers, whereas for the oblique valleys, the main effect is a slight increase of the QW band gap without much change in the relative band alignment. This is illustrated by the strained band diagrams depicted in Figs. 2(d) and 2(e).

To determine the exact band alignment, the calculated transition energies for the actual QW strain of  $\varepsilon_{\parallel, \text{QW}} = 0.3\%$  [dotted curves in Figs. 2(f) and 2(g)] are compared to the measured transitions, which are represented by the solid horizontal lines. Evidently, a simultaneous agreement for both the oblique and longitudinal transitions occurs only for a particular band offset value marked by the square symbols (■) in Fig. 2. This yields an *unstrained* conduction-band offset  $\Delta E_c/\Delta E_g = 0.45 \pm 0.05$ , i.e., a nearly symmetric unstrained band alignment for the PbTe/PbSrTe system. However, due to the epitaxial strain in the QWs, the band edges of the longitudinal valley are shifted downwards, as illustrated by the band diagrams depicted in Figs. 2(d) and 2(e). Thus, in the

strained QWs, the band alignment is asymmetric and, due to this asymmetry, the maxima of the longitudinal transitions are shifted to lower band offsets, whereas for the oblique valleys, the shift is rather small. It is emphasized that this different behavior strongly enhances the precision of the derived band offset value, as due to this asymmetry the data for both valleys only fits to the calculations for a unique band offset value.

The same analysis was performed for the PbSe/PbSrSe quantum wells, as shown in Figs. 3(e) and 3(f), where again the calculated transition energies for the highest QW transitions are plotted in dependence of the unstrained band offset for different strain values. Evidently, the effect of strain is much less pronounced than in the PbTe/PbSrTe system. This is explained by the smaller deformation potentials (see Table II) as well as the factor-of-two smaller strain in the PbSe system (see Table I). Thus, strain plays a less important role in the selenide than in the telluride system. From the comparison of calculation for  $\epsilon_{\parallel, \text{QW}} = 0.1\%$  with the experimental transition energies represented by the horizontal lines, we derive an unstrained band offset of  $\Delta E_c / \Delta E_g = 0.6 \pm 0.1$  for the PbSe/PbSrSe system. This means that the conduction-band offset is higher than in the PbTe/PbSrTe case. It is to be noted

that the larger error bar for the PbSe system is a consequence of the smaller strain-induced shifts of the electronic transitions, for which reason the band offset range where the calculations fit to the experimental values is larger than in the PbTe case.

Using the derived band parameters, the dependence of the interband transitions on QW thickness is presented in Fig. 4 for both systems for  $T = 80$  K and  $x_{\text{Sr}} \sim 13\%$ . In each plot, the blue and red colors correspond to the longitudinal and oblique valley transitions, respectively, revealing the large valley splitting in the PbTe QWs [Fig. 4(a)], whereas it is much smaller in the PbSe system [Fig. 4(b)]. Plotted on top of the calculations (solid lines) is the experimental data (symbols) obtained for the different samples, evidencing the excellent agreement between experiments and theoretical calculations for all samples. This underlines the consistency of our results and the reliability of our band offsets and envelope function model.

To check whether the band alignments depend on temperature, the same analysis was performed for the data measured at different temperatures. The results for 20 and 300 K are shown in Fig. 5, where the measured transitions (horizontal lines) are again compared to the theoretical calculations (symbols) as a

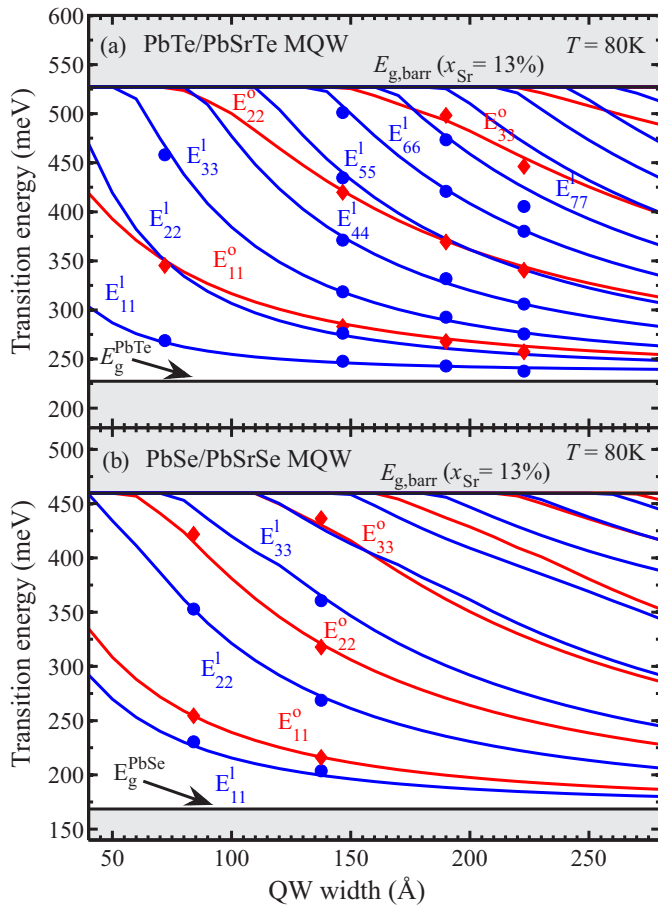


FIG. 4. (Color online) Transition energies of (a) PbTe/PbSrTe and (b) PbSe/PbSrSe MQWs as a function of quantum-well width at 80 K. Symbols  $\bullet$  and  $\blacklozenge$  represent the measured data of our samples (see Table I) and the solid lines represent the calculations using the envelope function model for  $x_{\text{Sr}} = 13\%$  and the band offsets and strain values  $\epsilon_{\parallel, \text{QW}} = 0.3$  and  $0.1\%$  derived from Figs. 1–3.

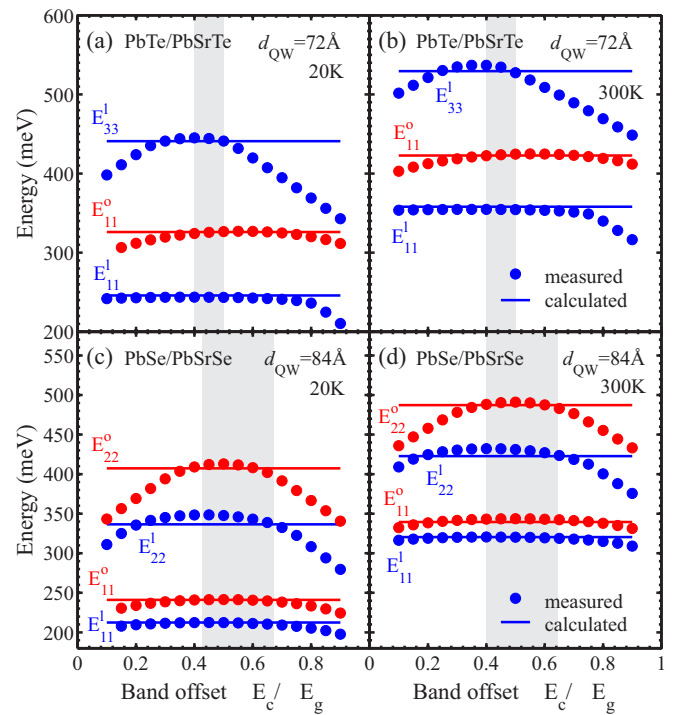


FIG. 5. (Color online) Transition energies of the QWs (symbols  $\bullet$ ) calculated as a function of the unstrained relative band offset  $\Delta E_c / \Delta E_g$  at 20 and 300 K (left- and right-hand side, respectively). (a),(b) PbTe/PbSrTe MQW with  $d_{\text{QW}} = 72$  Å; (c),(d) PbSe/PbSrSe MQW with  $d_{\text{QW}} = 84$  Å. The measured transition energies are represented by the solid horizontal lines and the sample parameters are listed in Table I. The transitions are labeled by  $E_{ii}^{l,o}$  where the indices  $i$  denotes the  $i$ th initial and final state in the QWs, and  $l$  and  $o$  denote the longitudinal and oblique valleys, respectively. The shaded regions mark the range of the band offset values within the error bounds, giving  $\Delta E_c / \Delta E_g = 0.45 \pm 0.05$  and  $0.6 \pm 0.1$  for the PbTe/PbSrTe and PbSe/PbSrSe systems independent of temperature.

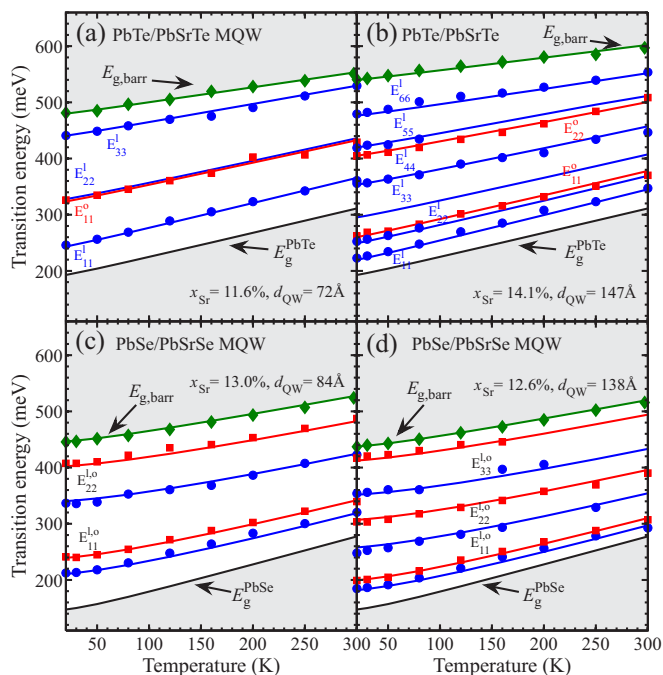


FIG. 6. (Color online) Measured (symbols ● and ■) and calculated (solid lines) temperature-dependent transition energies  $E_{ii}^{l,o}$  of two (a),(b) PbTe/PbSrTe and (c),(d) PbSe/PbSrSe MQWs with QW thicknesses of 72, 147, 84, and 138 Å, respectively, for a constant band offset of  $\Delta E_c/\Delta E_g = 0.45$  for PbTe/PbSrTe and  $\Delta E_c/\Delta E_g = 0.6$  for PbSe/PbSrSe, demonstrating an excellent agreement between theory and experiments at all temperatures. The shaded regions indicate the PbTe, PbSe and PbSrTe, PbSrSe band gaps for the given Sr contents  $x_{\text{Sr}}$  of 11.6%, 14.1%, 13.0%, and 12.6% as listed in Table I.

function of conduction-band offset for the PbTe/PbSrTe MQW with  $d_{\text{QW}} = 72$  Å (top) and the PbSe/PbSrSe MQW with  $d_{\text{QW}} = 84$  Å (bottom). Evidently, a good agreement between measurements and calculations is found at all temperatures for the same band offset  $\Delta E_c/\Delta E_g = 0.45$  and 0.6 for the PbTe/PbSrTe and PbSe/PbSrSe systems within the error indicated by the shaded areas. Thus, the band alignment is practically independent of temperature in both material systems. Figure 5 also demonstrates that only the highest-energy QW transitions close to  $E_g^{\text{barr}}$  are sensitive to the band

alignment, whereas the ground-state transitions  $E_{11}^{l,o}$  as seen, e.g., in photoluminescence measurements [24], do not depend much on the band offset value. Thus, such measurements are not at all suited for determination of the band alignments. As a further demonstration the temperature dependence of the measured transitions (symbols) is compared in Fig. 6 to the calculations (solid lines) for the whole temperature range from 20 to 300 K for four representative samples PbTe and PbSe QW samples. Clearly, the complete data set is in perfect agreement with the calculations, which underlines the reliability of our model parameters and band offset values deduced.

## VI. CONCLUSION

In summary, through systematic investigation of the optical transitions by temperature-modulated absorption spectroscopy and envelope function calculations, the band alignments of two of the most important IV-VI heterostructure systems were derived, giving a type-I band alignment with a relative unstrained conduction-band offset  $\Delta E_c/\Delta E_g = 0.45 \pm 0.05$  for the PbTe/PbSrTe and  $0.6 \pm 0.1$  for PbSe/PbSrSe systems for Sr contents up to 14%. Within the experimental error, the band offsets are independent of temperature between 20 and 300 K. Evaluation of the effect of strain revealed that it is important for the PbTe/PbSrTe but less significant for the PbSe/PbSrSe system. This is due to the larger lattice mismatch as well as the larger deformation potentials in the telluride system, where also the valley splitting in the is three times larger due to the higher effective mass anisotropy. The strain in the quantum wells induces a substantial downward shift of the band edges for the longitudinal  $L$  valleys, whereas the effect is much weaker for the oblique valleys. The resulting asymmetry in the conduction- and valence-band offset allows a more precise band alignment determination. With the derived band offset band parameters and the previous results obtained for the Eu-based quantum-well systems [20–22], we have thus established a unified parameter set for modeling of the electronic structure of the four most important IV-VI heterostructure systems that allows their realistic design for practical device applications.

## ACKNOWLEDGMENT

This work was supported by the Austrian Science Fund through the special research Program No. SFB-025 IR-ON.

- [1] Z. Shi, M. Tacke, A. Lambrecht, and H. Bottner, *Appl. Phys. Lett.* **66**, 2537 (1995).
- [2] G. Bauer, M. Kriechbaum, Z. Shi, and M. Tacke, *J. Nonlin. Opt. Phys. Mater.* **04**, 283 (1995).
- [3] U. P. Schiel and J. Rohr, *Infrared Phys. Technol.* **40**, 325 (1999).
- [4] W. Heiss, T. Schwarzl, G. Springholz, K. Biermann, and K. Reimann, *Appl. Phys. Lett.* **78**, 862 (2001).
- [5] C. L. Felix, W. W. Bewley, I. Vurgaftman, J. R. Lindle, J. R. Meyer, H. Z. Wu, G. Xu, S. Khosravani, and Z. Shi, *Appl. Phys. Lett.* **78**, 3770 (2001).
- [6] J. Frst, H. Pascher, T. Schwarzl, M. Böberl, W. Heiss, G. Springholz, and G. Bauer, *Appl. Phys. Lett.* **81**, 208 (2002).
- [7] F. Zhao, H. Wu, A. Majumdar, and Z. Shi, *Appl. Phys. Lett.* **83**, 5133 (2003).
- [8] M. Eibelhuber, T. Schwarzl, S. Pichler, W. Heiss, and G. Springholz, *Appl. Phys. Lett.* **97**, 061103 (2010).
- [9] A. Khiar, M. Rahim, M. Fill, F. Felder, F. Hobrecker, and H. Zogg, *Appl. Phys. Lett.* **97**, 151104 (2010).
- [10] M. Fill, A. Khiar, M. Rahim, F. Felder, and H. Zogg, *J. Appl. Phys.* **109**, 093101 (2011).
- [11] B. Weng, J. Ma, L. Wei, L. Li, J. Qiu, J. Xu, and Z. Shi, *Appl. Phys. Lett.* **99**, 221110 (2011).
- [12] F. Felder, M. Arnold, M. Rahim, C. Ebnetter, and H. Zogg, *Appl. Phys. Lett.* **91**, 101102 (2007).

- [13] M. Böberl, T. Fromherz, J. Roither, G. Pillwein, G. Springholz, and W. Heiss, *Appl. Phys. Lett.* **88**, 041105 (2006).
- [14] For a recent review, see G. Springholz and G. Bauer, *Landoldt-Börnstein*, Vol. III/34a, edited by C. Klingshirn (Springer, Berlin, 2013), pp. 415–561, and references therein.
- [15] D. Partin, *J. Vac. Sci. Technol. B* **5**, 686 (1987).
- [16] A. Lambrecht, N. Herres, B. Spanger, S. Kuhn, H. Böttner, M. Tacke, and J. Evers, *J. Cryst. Growth* **108**, 301 (1991).
- [17] N. Sakurai, H. Fujiyasu, and A. Ishida, *Japan. J. Appl. Phys.* **33**, 151 (1994).
- [18] H. Beyer, A. Lambrecht, J. Nurnus, H. Bottner, H. Griessmann, A. Heinrich, L. Schmitt, M. Blumers, and F. Volklein, in *Proceedings of the 18th International Conference on Thermoelectrics (ICT)* (IEEE, Baltimore, 1999), pp. 687–695.
- [19] E. A. de Andrada e Silva, *Phys. Rev. B* **60**, 8859 (1999).
- [20] S. Yuan, G. Springholz, G. Bauer, and M. Kriechbaum, *Phys. Rev. B* **49**, 5476 (1994).
- [21] M. Simma, T. Fromherz, G. Bauer, and G. Springholz, *Appl. Phys. Lett.* **95**, 212103 (2009).
- [22] M. Simma, G. Bauer, and G. Springholz, *Appl. Phys. Lett.* **101**, 172106 (2012).
- [23] H. Z. Wu, N. Dai, M. B. Johnson, P. J. McCann, and Z. S. Shi, *Appl. Phys. Lett.* **78**, 2199 (2001).
- [24] W. Z. Shen, K. Wang, L. F. Jiang, X. G. Wang, S. C. Shen, H. Z. Wu, and P. J. McCann, *Appl. Phys. Lett.* **79**, 2579 (2001).
- [25] W. Z. Shen, H. Z. Wu, and P. J. McCann, *J. Appl. Phys.* **91**, 3621 (2002).
- [26] K. Biswas, J. He, I. D. Blum, C.-I. Wu, T. P. Hogan, D. N. Seidman, V. P. Dravid, and M. G. Kanatzidis, *Nature (London)* **489**, 414 (2012).
- [27] Y. Lee, S.-H. Lo, J. Androulakis, C.-I. Wu, L.-D. Zhao, D.-Y. Chung, T. P. Hogan, V. P. Dravid, and M. G. Kanatzidis, *J. Am. Chem. Soc.* **135**, 5152 (2013).
- [28] J. He, M. G. Kanatzidis, and V. P. Dravid, *Mater. Today* **16**, 166 (2013).
- [29] T. H. Hsieh, H. Lin, J. Liu, W. Duan, A. Bansil, and L. Fu, *Nat. Commun.* **3**, 982 (2012).
- [30] P. Dziawa, B. J. Kowalski, K. Dybko, R. Buczko, A. Szczerbakow, M. Szot, E. Łusakowska, T. Balasubramanian, B. M. Wojek, M. H. Berntsen, O. Tjernberg, and T. Story, *Nat. Mater.* **11**, 1023 (2012).
- [31] Y. Tanaka, Z. Ren, T. Sato, K. Nakayama, S. Souma, T. Takahashi, K. Segawa, and Y. Ando, *Nat. Phys.* **8**, 800 (2012).
- [32] S.-Y. Xu, C. Liu, N. Alidoust, M. Neupane, D. Qian, I. Belopolski, J. D. Denlinger, Y. J. Wang, H. Lin, L. A. Wray, G. Landolt, B. Slomski, J. H. Dil, A. Marcinkova, E. Morosan, Q. Gibson, R. Sankar, F. C. Chou, R. J. Cava, A. Bansil, and M. Z. Hasan, *Nat. Commun.* **3**, 1192 (2012).
- [33] R. Buczko and L. Cywiński, *Phys. Rev. B* **85**, 205319 (2012).
- [34] G. Yang, J. Liu, L. Fu, W. Duan, and C. Liu, *Phys. Rev. B* **89**, 085312 (2014).
- [35] H. Wu, N. Dai, and P. J. McCann, *Phys. Rev. B* **66**, 045303 (2002).
- [36] R. C. Miller, A. C. Gossard, D. A. Kleinman, and O. Munteanu, *Phys. Rev. B* **29**, 3740 (1984).
- [37] H. Pascher, G. Bauer, and R. Grisar, *Phys. Rev. B* **38**, 3383 (1988).
- [38] P. Röhlein, H. Pascher, G. Bauer, and M. Tacke, *Semicond. Sci. Technol.* **5**, S147 (1990).
- [39] T. Maurice, F. Mahoukou, G. Breton, S. Charar, P. Masri, M. Averous, and R. Bisaro, *Phys. Status Solidi B* **209**, 523 (1998).
- [40] G. Springholz, in *Molecular Beam Epitaxy*, edited by M. Henini (Elsevier, Waltham, MA, 2013), pp. 263–310.
- [41] H. G. Zimmer, H. Winzen, and K. Syassen, *Phys. Rev. B* **32**, 4066 (1985).
- [42] F. Marinelli, H. Dupin, and A. Lichanot, *J. Phys. Chem. Solids* **61**, 1707 (2000).
- [43] S. W. McKnight, K. P. Stewart, H. D. Drew, and K. Moorjani, *Infrared Phys.* **27**, 327 (1987).
- [44] K. Syassen, N. E. Christensen, H. Winzen, K. Fischer, and J. Evers, *Phys. Rev. B* **35**, 4052 (1987).
- [45] Y. Kaneko and T. Koda, *J. Cryst. Growth* **86**, 72 (1988).
- [46] S. Rabi, *Phys. Rev.* **167**, 801 (1968).
- [47] I. I. Zasavitskii, E. A. de Andrada e Silva, E. Abramof, and P. J. McCann, *Phys. Rev. B* **70**, 115302 (2004).